

Orbital and Spin Dynamics of Single Neutrally-Charged Nitrogen-Vacancy Centers in Diamond

Baier, S.; Bradley, C.E.; Middelburg, T.; Dobrovitski, V.V.; Taminiau, T.H.; Hanson, R.

DOI

[10.1103/PhysRevLett.125.193601](https://doi.org/10.1103/PhysRevLett.125.193601)

Publication date

2020

Document Version

Final published version

Published in

Physical Review Letters

Citation (APA)

Baier, S., Bradley, C. E., Middelburg, T., Dobrovitski, V. V., Taminiau, T. H., & Hanson, R. (2020). Orbital and Spin Dynamics of Single Neutrally-Charged Nitrogen-Vacancy Centers in Diamond. *Physical Review Letters*, 125(19), Article 193601. <https://doi.org/10.1103/PhysRevLett.125.193601>

Important note

To cite this publication, please use the final published version (if applicable). Please check the document version above.

Copyright

Other than for strictly personal use, it is not permitted to download, forward or distribute the text or part of it, without the consent of the author(s) and/or copyright holder(s), unless the work is under an open content license such as Creative Commons.

Takedown policy

Please contact us and provide details if you believe this document breaches copyrights. We will remove access to the work immediately and investigate your claim.

Orbital and Spin Dynamics of Single Neutrally-Charged Nitrogen-Vacancy Centers in Diamond

S. Baier^{1,2,*}, C. E. Bradley^{1,2,‡}, T. Middelburg^{1,2}, V. V. Dobrovitski^{1,2}, T. H. Taminiau^{1,2} and R. Hanson^{1,2,†}

¹QuTech, Delft University of Technology, 2628 CJ Delft, Netherlands

²Kavli Institute of Nanoscience, Delft University of Technology, 2628 CJ Delft, Netherlands



(Received 30 July 2020; accepted 2 October 2020; published 4 November 2020)

The neutral charge state plays an important role in quantum information and sensing applications based on nitrogen-vacancy centers. However, the orbital and spin dynamics remain unexplored. Here, we use resonant excitation of single centers to directly reveal the fine structure, enabling selective addressing of spin-orbit states. Through pump-probe experiments, we find the orbital relaxation time (430 ns at 4.7 K) and measure its temperature dependence up to 11.8 K. Finally, we reveal the spin relaxation time (1.5 s) and realize projective high-fidelity single-shot readout of the spin state ($\geq 98\%$).

DOI: [10.1103/PhysRevLett.125.193601](https://doi.org/10.1103/PhysRevLett.125.193601)

Defect centers in solids are a promising class of systems for quantum science and technology [1,2]. They combine bright optical transitions, access to long-lived electronic- and nuclear-spin registers, and compatibility with solid-state device engineering. Of particular prominence is the negatively-charged nitrogen-vacancy center (NV^-) in diamond, which has enabled recent advances in quantum information science [3,4] and quantum sensing [5–7].

Alongside NV^- , the nitrogen-vacancy defect can exist in both the neutral- (NV^0) and—with sufficient Fermi-level engineering—positive- (NV^+) charge states. These additional charge states can be used as a resource in a number of applications, such as spin-to-charge conversion for improved spin-state readout [8,9], classical data storage in NV ensembles [10], and deliberate charge-state switching for improved nuclear-spin coherence under ambient conditions [11,12].

Conversely, for experiments based upon NV^- , undesired conversion to NV^0 can be a hindrance: Active charge-state initialization protocols have been used to counter this [13,14]. For quantum networks, stochastic conversion from NV^- to NV^0 is an important decoherence mechanism for nuclear-spin quantum memories [15].

Despite the importance of NV^0 , understanding of many of its properties remains elusive. In particular, the orbital- and spin-dynamic timescales are unknown. Also, while recent magnetic circular dichroism (MCD) measurements on ensembles [16,17] give insight into the NV^0 fine structure, no direct observation has been reported.

Building an understanding of the system and its associated dynamic processes is important for improving control in NV quantum devices. Moreover, the knowledge gained may offer new insights into the physics of other impurities in solids [18]. Finally, NV^0 may prove to be a powerful quantum system in its own right.

Here, we develop protocols combining resonant excitation of both NV^0 and NV^- . We apply these novel protocols to reveal the orbital and spin dynamics of single NV^0 centers in diamond as well as to realize initialization and single-shot readout of the NV^0 spin state. We perform our measurements on single NV centers at cryogenic temperatures [19]; see Fig. 1(a). The NV center is addressed with microwave (mw) pulses (NV^- ground-state spin transitions) as well as with polarization-controlled $\lambda_{\text{red}} = 637$ nm [NV^- zero-phonon line (ZPL)] and $\lambda_{\text{yellow}} = 575$ nm (NV^0 ZPL) laser light. We apply an axial magnetic field of $B_z = 1890(5)$ G to induce significant Zeeman splitting.

The ZPL of the NV^0 center has been conclusively attributed to this defect [26–31]. A combination of *ab initio* calculations and symmetry arguments led to the proposal of ground states of 2E symmetry, which can be optically excited to a 2A_2 manifold [32,33]. An additional metastable 4A_2 quartet state was also predicted and has been observed by electron paramagnetic resonance (EPR) measurements under excitation of the NV^0 ZPL [34]. A splitting of the transitions of the two orbital states E_x and E_y has been measured [33,35]. However, the associated fine structure has not been observed in PL or EPR measurements.

We start by performing spectroscopy using the experimental procedure sketched in Fig. 1(b). For each frequency step, we (1) probabilistically prepare the emitter in NV^0 by applying strong laser excitation resonant with the NV^- ZPL, in combination with weak mw driving [19] to induce the conversion $NV^- \rightarrow NV^0$. We then (2) apply polarized

Published by the American Physical Society under the terms of the [Creative Commons Attribution 4.0 International license](https://creativecommons.org/licenses/by/4.0/). Further distribution of this work must maintain attribution to the author(s) and the published article's title, journal citation, and DOI.

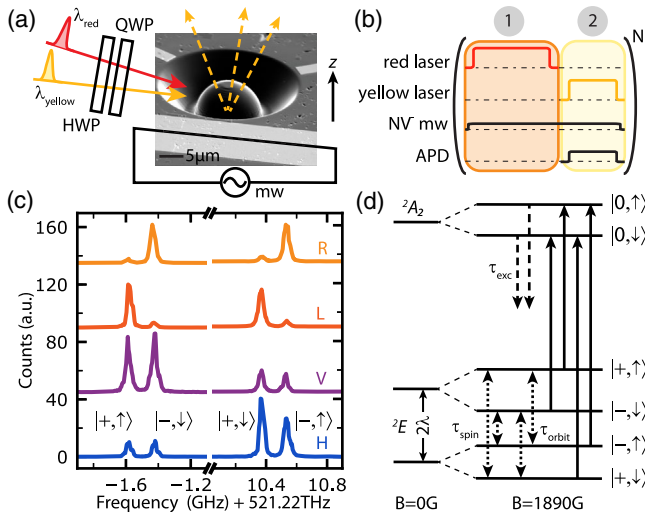


FIG. 1. Direct observation of the fine structure of the NV^0 center. (a) Electron microscope image of a solid immersion lens fabricated around the NV center. Optical (λ_{yellow} , λ_{red}) and mw control are indicated. (b) Experimental sequence for spectroscopy consisting of a preparation (1) and measurement (2) part. (c) Spectra obtained with linear (H , V) and circular (L , R) polarizations ($P_{\text{yellow}} = 500$ pW), offset for clarity [19]. (d) Ground- and excited-state level structure. Spin-conserving optical transitions (solid arrows), excited-state decay (dashed arrows), and spin or orbital relaxations (dotted arrows) are indicated.

yellow light, during which time all single photons above 650 nm are integrated.

The measured spectra [Fig. 1(c)] show four transitions—the first direct spectroscopic observation of the NV^0 fine structure. These observations validate the model of Barson *et al.* [16], and we hence follow their theoretical description below. Under the secular approximation, the ground-state Hamiltonian of NV^0 can be described by

$$H = g\mu_B\hat{S}_zB_z + l\mu_B\hat{L}_zB_z + 2\lambda\hat{L}_z\hat{S}_z + \epsilon_{\perp}(\hat{L}_- + \hat{L}_+). \quad (1)$$

g is the spin g factor, μ_B is the Bohr magneton, l is the orbital g factor, λ is the spin-orbit interaction parameter, and ϵ_{\perp} is the perpendicular strain parameter. $\hat{L}_z = \sigma_z$ and $\hat{S}_z = \frac{1}{2}\sigma_z$ are the orbital and spin operators, respectively, defined in terms of the Pauli matrix σ_z , while $\hat{L}_{\pm} = |\pm\rangle\langle\mp|$ with $|\pm\rangle = \mp[1/\sqrt{2}(|X\rangle \pm i|Y\rangle)]$ are the orbital operators defined within the basis of the strain eigenstates $\{|X\rangle, |Y\rangle\}$. The z axis is defined parallel to the NV axis.

The resulting level structure is presented in Fig. 1(d). The 2E ground state is composed of a pair of doublet states with opposite spin-orbit parity (lower spin-orbit branch: $\{|+\downarrow\rangle, |-\uparrow\rangle\}$; upper spin-orbit branch: $\{|-\downarrow\rangle, |+\uparrow\rangle\}$). The degeneracy of each doublet is lifted by orbital- and spin-Zeeman contributions under the applied magnetic field. Conversely, the 2A_2 excited state exhibits no

spin-orbit structure but is rather split by the spin-Zeeman effect alone. These contributions lead to four spin-conserving transitions. The contributing ground state for each observed transition is indicated in Fig. 1(c).

We find that the luminescence of the transitions depends significantly on the polarization of the excitation light [see Fig. 1(c)]. Differing transition amplitudes for orthogonal polarizations can be attributed to optical selection rules that are strongly dependent on ϵ_{\perp} [16,19]. Based upon these observations, we develop a method to extract ϵ_{\perp} and simultaneously the fine structure parameters of the NV^0 Hamiltonian [19]. By fitting spectra from three individual NV centers against our theoretical model, we find $l = 0.039(11)$ and $\lambda = 4.9(4)$ GHz. These values are roughly a factor of 2 larger than those found previously using NV-ensemble MCD measurements [36].

Crucially, the data in Fig. 1(c) show that resonant optical excitation in this magnetic field regime allows for state-resolved addressing, enabling the heralded preparation of specific states and investigation of the system dynamics. To date, only the excited-state lifetime τ_{exc} of 21 ns has been reported [38]. Here, we investigate the orbital- and spin-relaxation timescales of the ground state, τ_{orbit} and τ_{spin} , respectively; see Fig. 1(d).

In order to unambiguously measure the dynamics of NV^0 , we design and implement a charge-resonance (CR) protocol that realizes high-fidelity heralded preparation into NV^0 , with the $\lambda = 575$ nm laser resonant with a chosen optical transition; see Fig. 2(a). The CR protocol (1) can be broken down as follows. First, a heralding signal confirms preparation in NV^- , with the $\lambda = 637$ nm lasers on resonance with the NV^- transitions. Next, a strong red optical pulse induces charge state conversion, after which a chosen NV^0 transition is excited with yellow light. If the photon counts obtained during the “ NV^0 check” exceed a preset threshold, the protocol is completed. Further details are given in Supplemental Material [19].

After the CR protocol, we perform the experimental sequence on NV^0 (2). Finally, we detect whether undesired conversion to NV^- occurred during the experimental sequence and then perform readout of the NV^0 state (3). The number of repetitions of the experimental sequence (2) is chosen to minimize the overhead from the CR protocol while maintaining an NV^0 population above 85% and ranges from $N = 15$ to 1000 dependent upon the used yellow power. Note that the CR protocol prepares a specific spin state of the NV^0 center. For circular polarization, we typically start the experiment by heralding the $|\downarrow\rangle$ spin state. For linear polarization, however, due to their close spectral vicinity, the CR check heralds either the $|\downarrow\rangle$ or $|\uparrow\rangle$ spin state.

In Fig. 2(b), we show time-resolved pump measurements. Here, the yellow laser is gated by an acousto-optic modulator (AOM), with a measured rise and fall time of 30(5) and 7(1) ns, respectively. Upon opening the AOM,

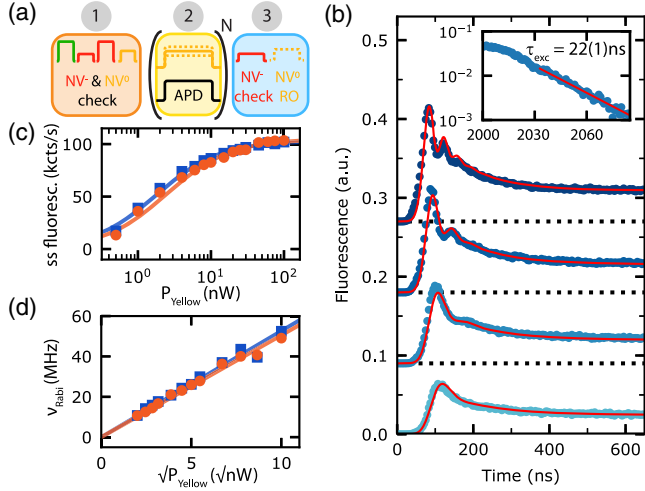


FIG. 2. Time-resolved resonant pump measurements. (a) Experimental sequence consisting of preparation (1), measurement (2), and readout (3) parts. (b) Fluorescence of NV^0 when driving the lower spin-orbit branch with H polarization for $P_{\text{yellow}} = 2, 4, 10, 20\text{ nW}$ (bottom to top) averaged over at least 1×10^6 repetitions. Measurements have a timing resolution of 250 ps and are offset for clarity. Solid red lines are simulations of the full system dynamics with our theoretical model [19]. Inset: Decay of fluorescence counts after the AOM is closed. (c) Steady-state (ss) fluorescence counts as a function of P_{yellow} , for H (squares) and L polarization (circles). The data are fit with a saturation curve $f(P) = A[P/(P + P_{\text{sat}})]$. (d) Optical Rabi frequency as a function of $\sqrt{P_{\text{yellow}}}$. Fits yield a slope of $5.3(1)/5.1(1)$ MHz/ $\sqrt{\text{nW}}$ for L/H polarization.

we observe a rapid increase in fluorescence due to optical cycling, which is then damped as population is pumped out of the driven state. By fitting the steady-state fluorescence counts for L (H) polarization, we extract a saturation power of $2.5(2)$ [$1.8(1)$] nW and saturation counts of $105(2)$ [$103(2)$] kcts/s; see Fig. 2(c). As the optical power is increased, coherent optical Rabi oscillations are observed. In Fig. 2(d), we plot the fitted frequency of these oscillations, revealing the expected $\sqrt{P_{\text{yellow}}}$ dependence. When the AOM is closed, the fluorescence decays with $\tau_{\text{exc}} = 22(1)$ ns [inset in Fig. 2(b)], which is consistent with the literature [38].

To uncover the recovery timescale after pumping, we turn to pump-probe spectroscopy. Example time traces are shown in Fig. 3(a). The resulting data are well described by an exponential recovery with a single timescale associated with how fast the system relaxes [19] once illumination is turned off. At the base temperature of our cryostat [$T = 4.65(3)$ K], we extract $\tau_{\text{recovery}} = 0.43(6)$ μs . We attribute these fast dynamics to orbital relaxation processes, i.e., $|+\rangle \leftrightarrow |-\rangle$ and $\tau_{\text{orbit}} = \tau_{\text{recovery}}$.

We repeat the pump-probe measurements across a range of temperatures. The fitted recovery times are shown as rates $R_{\text{recovery}} = 1/t_{\text{recovery}}$ in Fig. 3(b). After an initial

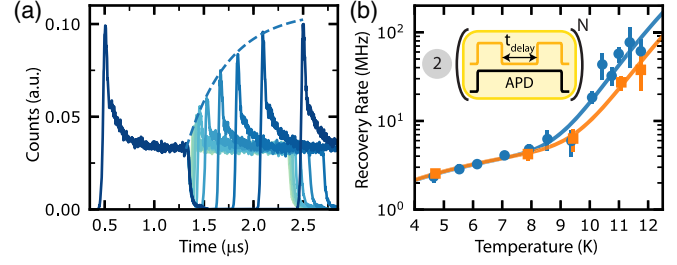


FIG. 3. Time-resolved pump-probe spectroscopy. The experimental sequence after state preparation is given in the inset in (b). (a) Example traces for a range of t_{delay} (light to dark for increasing t_{delay}), at a temperature of $5.5(1)$ K, integrated over 5×10^6 acquisitions each, measured with H polarization. The dashed line is a fit to the recovery behavior [19]. (b) Recovery rate R_{recovery} as a function of the cryostat temperature. Circles (squares) describe data measured on the lower (upper) spin-orbit branch. Error bars for R_{recovery} correspond to 1 s.d. fit errors. The solid lines are fits of form $f(T) = AT + B \exp[-\Delta/k_B T]$, giving $A = 0.53(3)$ MHz/K [$A = 0.54(2)$ MHz/K] and $B = 1(1) \times 10^7$ MHz [$B = 1(4) \times 10^7$ MHz] for the lower (upper) branch.

linear increase, a rapid increase is observed at higher temperatures. At these higher temperatures, the required time resolution exceeds the AOM switching time constants, which we take into account in the fitting procedure [19].

The initial linear increase ($\propto T$) can be attributed to single-phonon processes, while high-order processes appear to govern the recovery rate at higher temperatures [39,40]. Here, we fit individually to a two-phonon Raman process ($\propto T^n$) and a two-phonon Orbach process ($\propto \exp[-\Delta/k_B T]$), with k_B being the Boltzmann constant. For the Raman process, the fit returns $n = 13(2)$ [$14(3)$] for the lower (upper) spin-orbit branch; a physical explanation for such values is currently lacking. For the Orbach process, we find a characteristic energy scale of $\Delta = 12(2)$ meV [$\Delta = 13(4)$ meV] extracted from a fit to the lower (upper) spin-orbit branch. Δ is associated to the energy splitting to the first vibronic level of the NV^0 ground state, predicted to be a Jahn-Teller system [26,41]. The value found here agrees with the bulk absorption measurements of Davies [26] [$13.6(7)$ meV] and with recent density-functional theory calculations (21.4 meV) [41], suggesting that the measured increase of R_{recovery} is predominantly due to two-phonon Orbach processes. While a detailed model is beyond the scope of this work, we expect that our findings will aid in the further understanding of the vibronic structure of NV^0 .

Now we turn to the spin dynamics of NV^0 . Here, we exploit polarization control to selectively prepare, address, and read out the NV^0 spin state. These measurements are all performed on timescales $\gg \tau_{\text{orbit}} = 0.43(6)$ μs and, thus, average over the orbital basis; we will therefore refer only to the spin states. In all experiments below, we use L polarization, addressing the $|\downarrow\rangle$ state. We herald the

preparation of $|\downarrow\rangle$ by applying 25 nW for 250 μ s and proceed when more than 25 photons are detected. After a delay of 0.1 ms, we perform a charge-state check with red excitation, followed by a second yellow readout (again, 25 nW for 250 μ s); see Fig. 2(a) (3). We then repeat this experiment, but with a delay of 10 s between the yellow readouts, allowing for relaxation processes to occur. The resulting histograms are shown in Fig. 4(a).

In the first case (dark colors), we observe a single dominant population which can be modeled by a Poissonian distribution with mean photon count 25.2(2) and that we attribute to $|\downarrow\rangle$. In the second case (light colors), we additionally observe a second distribution, again modeled as a Poissonian distribution with mean photon count 0.171(4). A charge-state measurement of NV^- performed before each readout shows that only a small fraction of the population ($P_{NV^-} \sim 1\%$) is found in the unwanted charge state—which we discard from the histograms—and that the majority of low-count events can be attributed to a dark state of NV^0 . As the populations evolve without laser excitation, the dark state must be part of the ground-state manifold; we therefore assign this state to the second spin state $|\uparrow\rangle$. A readout threshold of five photons [solid line, Fig. 4(a)] discriminates the two spin states.

We now sweep the delay time between initialization and readout. The measured populations of $|\downarrow\rangle$ (P_\downarrow) and $|\uparrow\rangle$ (P_\uparrow) are plotted in Fig. 4(b), showing relaxation to a mean population of 0.494(6). The data are consistent with a

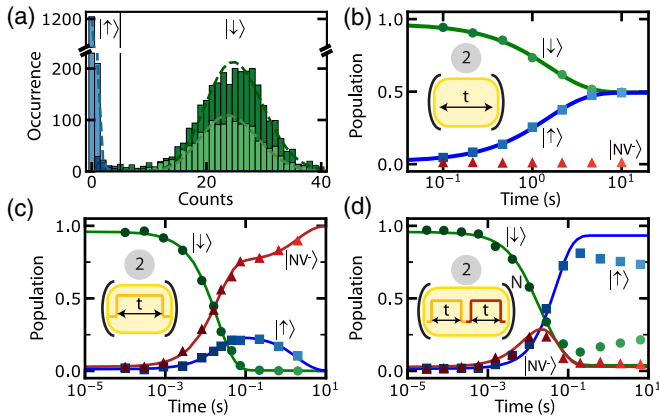


FIG. 4. Single-shot readout and spin pumping. (a) Histograms after preparation of the NV^0 $|\downarrow\rangle$ state (dark colors) and mixed (light colors) spin states. (b) Relaxation (T_1) measurement for the $|\downarrow\rangle$ (circles) and $|\uparrow\rangle$ (squares) states, fitted with an exponential decay (recovery). The NV^- population (triangles) remains negligible in the dark. The data are averaged over 3×10^3 repetitions each. (c) Spin pumping: NV^0 spin and total NV^- populations as a function of yellow illumination time. Solid lines are fits to solutions for the underlying three-level rate equations [19]. (d) Spin pumping with charge cycling: the same as (c) but with stroboscopic red illumination. The time axis is the yellow illumination time (half of the total sequence time).

spin-1/2 T_1 process of characteristic timescale $\tau_{\text{spin}} = 1.51(1)$ s. Note that the observed value is a lower bound of the intrinsic spin relaxation, as it may be limited by leakage of resonant laser light. By setting the initial and long-time population in $|\downarrow\rangle$ to be 1 and 0.5, respectively, we obtain a lower bound for the single-shot readout fidelity, $F_{\text{RO}} = \frac{1}{2}(F_{|\downarrow\rangle} + F_{|\uparrow\rangle}) \geq 98.2(9)\%$, where $F_{|s\rangle}$ is the probability to assign $|s\rangle$ after preparing $|s\rangle$ [19].

To investigate the cycling nature of the driven optical transition, we now repeat the measurement under 5 nW of resonant yellow excitation; see Fig. 4(c). We find that P_\downarrow decreases on a timescale faster than can be explained by spin relaxation alone, showing that the optical excitation induces spin pumping. Possible spin-mixing channels are given either in the 2A_2 excited state or via an intersystem crossing, which might be offered by the 4A_2 state. We also find a significant increase of P_{NV^-} due to optically induced charge conversion [19,42]. However, this slows once $|\downarrow\rangle$ is depleted, as $|\uparrow\rangle$ is a dark state for optical excitation. Beyond this, P_\uparrow reduces with τ_{spin} , and charge conversion continues. We find a high state preparation fidelity for $|\uparrow\rangle$ of $99_{-10}^{+1}\%$ after 600 ms but with an absolute population in the NV^0 $|\uparrow\rangle$ state of only 22(2)%.

To reveal the respective rates, we develop a three-level rate equation model that we fit to our data, using the measured spin-relaxation time as a fixed input [solid lines, Fig. 4(c)] [19]. For the applied power of 5 nW, we extract characteristic timescales of 27(1) ms [90(4) ms] for the charge conversion (spin-pumping) process. From this, we can estimate the cyclicity of the $|\downarrow\rangle$ state within this regime to be $0.98(8) \times 10^5$ cycles, mainly limited by recharging to NV^- [19].

In a second experiment, the 5 nW yellow excitation is stroboscopically interleaved with strong $NV^- \rightarrow NV^0$ ionization pulses [19]; see Fig. 4(d). Again, we observe a gradual decrease of P_\downarrow and an increase of both P_\uparrow and P_{NV^-} , but then P_{NV^-} growth stops and even inverts. This observation can be explained via the picture that the removal of an electron from NV^- prepares a random spin state in NV^0 , eventually populating the dark state $|\uparrow\rangle$. Competing rates between this spin-selection process and spin relaxation lead to the observed steady-state populations. We again fit a three-level rate equation model, using the previously obtained parameters as fixed inputs [19], and extract a timescale for ionization of 18(4) ms. The rate equation model does not accurately describe the behavior at long timescales, which is likely due to a reduction of the NV^0 spin-relaxation time under red excitation and strong NV^- microwave driving [19].

As a final step, we develop a master equation simulation to capture the full dynamics of the NV^0 center [19]. In Fig. 2(b), we plot the simulated excited-state population (solid line), using the uncovered NV^0 timescales and spectral properties. We match the Rabi frequency to the

measured optical power and further include a spectral average over a Gaussian distribution of detuning values with $\text{FWHM} = 2\pi \times 20$ MHz. We find excellent agreement with our experimental fluorescence data, emphasizing a consistent understanding of the NV^0 dynamics.

In conclusion, we have developed a novel toolbox for the study and control of single neutrally-charged NV centers in diamond. We have uncovered the dynamic timescales and demonstrated single-shot readout and initialization by measurement of the NV^0 spin, each with high fidelity. In future investigations, coherent control of the spin states may be obtained. Detailed modeling of the defect may give new insights into the observed temperature dependence of the orbital dynamics. On the application side, protection of nuclear spin quantum memories from dephasing by NV^0 may be achieved by microwave spin locking in both orbitals or by feedback based upon the NV^0 spin readout demonstrated here. Finally, at reduced temperatures that suppress the orbital dynamics, NV^0 may prove to be a powerful system for quantum technologies in its own right.

We thank Michael Barson, Marcus Doherty, and Neil Manson for fruitful discussions. Furthermore, we thank Matteo Pompili, Sophie Hermans, and Hans Beukers for experimental assistance and Joe Randall, Maximilian Ruf, and Matteo Pasini for reviewing the manuscript. We acknowledge financial support from the EU Flagship on Quantum Technologies project Quantum Internet Alliance, the Netherlands Organisation for Scientific Research (NWO) through a Vici grant, a Vidi grant (Project No. 680-47-552) and within the research program NWO QuTech Physics Funding (QTECH, program 172, Project No. 16QTECH02), the Zwaartekracht Grant Quantum Software Consortium (Project No. 024.003.037/3368), and the European Research Council (ERC) through an ERC Consolidator Grant and an ERC starting grant (Grant Agreement No. 852410). S.B. is supported within an Erwin-Schrödinger fellowship (QuantNet, No. J 4229-N27) of the Austrian National Science Foundation (FWF).

*Corresponding author.
s.baier@tudelft.nl

†Corresponding author.
r.hanson@tudelft.nl

‡These authors contributed equally to this work.

- [1] M. Atatüre, D. Englund, N. Vamivakas, S.-Y. Lee, and J. Wrachtrup, *Nat. Rev. Mater.* **3**, 38 (2018).
- [2] D. D. Awschalom, R. Hanson, J. Wrachtrup, and B. B. Zhou, *Nat. Photonics* **12**, 516 (2018).
- [3] P. C. Humphreys, N. Kalb, J. P. J. Morits, R. N. Schouten, R. F. L. Vermeulen, D. J. Twitchen, M. Markham, and R. Hanson, *Nature (London)* **558**, 268 (2018).
- [4] C. E. Bradley, J. Randall, M. H. Abobeih, R. C. Berrevoets, M. J. Degen, M. A. Bakker, M. Markham, D. J. Twitchen, and T. H. Taminiau, *Phys. Rev. X* **9**, 031045 (2019).
- [5] N. Aslam, M. Pfender, P. Neumann, R. Reuter, A. Zappe, F. Fávoro de Oliveira, A. Denisenko, H. Sumiya, S. Onoda, J. Isoya, and J. Wrachtrup, *Science* **357**, 67 (2017).
- [6] D. R. Glenn, D. B. Bucher, J. Lee, M. D. Lukin, H. Park, and R. L. Walsworth, *Nature (London)* **555**, 351 (2018).
- [7] M. Abobeih, J. Randall, C. Bradley, H. Bartling, M. Bakker, M. Degen, M. Markham, D. Twitchen, and T. Taminiau, *Nature (London)* **576**, 411 (2019).
- [8] B. J. Shields, Q. P. Unterreithmeier, N. P. de Leon, H. Park, and M. D. Lukin, *Phys. Rev. Lett.* **114**, 136402 (2015).
- [9] D. A. Hopper, H. J. Shulevitz, and L. C. Bassett, *Micromachines* **9**, 437 (2018).
- [10] S. Dhomkar, J. Henshaw, H. Jayakumar, and C. A. Meriles, *Sci. Adv.* **2**, e1600911 (2016).
- [11] P. C. Maurer, G. Kucsko, C. Latta, L. Jiang, N. Y. Yao, S. D. Bennett, F. Pastawski, D. Hunger, N. Chisholm, M. Markham, D. J. Twitchen, J. I. Cirac, and M. D. Lukin, *Science* **336**, 1283 (2012).
- [12] M. Pfender *et al.*, *Nano Lett.* **17**, 5931 (2017).
- [13] H. Bernien, B. Hensen, W. Pfaff, G. Koolstra, M. S. Blok, L. Robledo, T. H. Taminiau, M. Markham, D. J. Twitchen, L. Childress, and R. Hanson, *Nature (London)* **497**, 86 (2013).
- [14] D. A. Hopper, J. D. Lauigan, T.-Y. Huang, and L. C. Bassett, *Phys. Rev. Applied* **13**, 024016 (2020).
- [15] N. Kalb, P. C. Humphreys, J. J. Slim, and R. Hanson, *Phys. Rev. A* **97**, 062330 (2018).
- [16] M. S. Barson, E. Krausz, N. B. Manson, and M. W. Doherty, *Nanophotonics* **8**, 1985 (2019).
- [17] D. Braukmann, E. R. Glaser, T. A. Kennedy, M. Bayer, and J. Debus, *Phys. Rev. B* **97**, 195448 (2018).
- [18] L. C. Bassett, A. Alkauskas, A. L. Exarhos, and K.-M. C. Fu, *Nanophotonics* **8**, 1867 (2019).
- [19] See Supplemental Material at <http://link.aps.org/supplemental/10.1103/PhysRevLett.125.193601> for details on the experimental measurements, theoretical models and analysis procedures, which includes Refs. [20–25].
- [20] J. P. Hadden, J. P. Harrison, A. C. Stanley-Clarke, L. Marseglia, Y.-L. D. Ho, B. R. Patton, J. L. O'Brien, and J. G. Rarity, *Appl. Phys. Lett.* **97**, 241901 (2010).
- [21] H. Bernien, Control, measurement and entanglement of remote quantum spin registers in diamond, Ph.D. Thesis, Delft University of Technology, 2014.
- [22] M. W. Doherty, N. B. Manson, P. Delaney, F. Jelezko, J. Wrachtrup, and L. C. L. Hollenberg, *Phys. Rep.* **528**, 1 (2013).
- [23] N. B. Manson, M. Hedges, M. S. J. Barson, R. Ahlefeldt, M. W. Doherty, H. Abe, T. Ohshima, and M. J. Sellars, *New J. Phys.* **20**, 113037 (2018).
- [24] J. J. Olivero and R. Longbothum, *J. Quant. Spectrosc. Radiat. Transfer* **17**, 233 (1977).
- [25] L. Robledo, H. Bernien, I. van Weperen, and R. Hanson, *Phys. Rev. Lett.* **105**, 177403 (2010).
- [26] G. Davies, *J. Phys. C* **12**, 2551 (1979).
- [27] Y. Mita, *Phys. Rev. B* **53**, 11360 (1996).
- [28] T. A. Kennedy, J. S. Colton, J. E. Butler, R. C. Linares, and P. J. Doering, *Appl. Phys. Lett.* **83**, 4190 (2003).
- [29] T. Gaebel, M. Domhan, C. Wittmann, I. Popa, F. Jelezko, J. Rabeau, A. Greentree, S. Prawer, E. Trajkov, P. R. Hemmer *et al.*, *Appl. Phys. B* **82**, 243 (2006).

- [30] G. Waldherr, J. Beck, M. Steiner, P. Neumann, A. Gali, T. Frauenheim, F. Jelezko, and J. Wrachtrup, *Phys. Rev. Lett.* **106**, 157601 (2011).
- [31] N. Aslam, G. Waldherr, P. Neumann, F. Jelezko, and J. Wrachtrup, *New J. Phys.* **15**, 013064 (2013).
- [32] A. Gali, *Phys. Rev. B* **79**, 235210 (2009).
- [33] N. B. Manson, K. Beha, A. Batalov, L. J. Rogers, M. W. Doherty, R. Bratschitsch, and A. Leitenstorfer, *Phys. Rev. B* **87**, 155209 (2013).
- [34] S. Felton, A. M. Edmonds, M. E. Newton, P. M. Martineau, D. Fisher, and D. J. Twitchen, *Phys. Rev. B* **77**, 081201(R) (2008).
- [35] B. J. Hensen, Quantum nonlocality with spins in diamond, Ph.D. Thesis, Delft University of Technology, 2016.
- [36] A reassessment of the procedures of Barson *et al.* concluded that it cannot be excluded that an error in documenting the data is the cause of this discrepancy [37].
- [37] M. Barson, ANU Canberra, Australia (private communication).
- [38] K. Beha, A. Batalov, N. B. Manson, R. Bratschitsch, and A. Leitenstorfer, *Phys. Rev. Lett.* **109**, 097404 (2012).
- [39] R. Orbach and B. Bleaney, *Proc. R. Soc. A* **264**, 458 (1961).
- [40] A. Abragam and B. Bleaney, *Electron Paramagnetic Resonance of Transition Ions* (Oxford University Press, Oxford, 2012).
- [41] J. Zhang, C.-Z. Wang, Z. Zhu, Q. H. Liu, and K.-M. Ho, *Phys. Rev. B* **97**, 165204 (2018).
- [42] P. Siyushev, H. Pinto, M. Vörös, A. Gali, F. Jelezko, and J. Wrachtrup, *Phys. Rev. Lett.* **110**, 167402 (2013).